VIII. TUBE RESEARCH AND DEVELOPMENT

A. MAGNETRON DEVELOPMENT

Dr. S. T. Martin
A. G. Barrett

1. Testing and Design of High-Power 10.7-Cm Magnetrons

Two more magnetrons have been assembled; one of them, MF-9B, was a salvaged anode assembly. Both tubes were unsuccessful. In the case of MF-11B, the ceramic window cracked at a late stage in leak-testing the assembly, while a bad leak developed in MF-9B during bakeout so that emission was too poor to allow operation. One of the magnetrons previously processed, MF-12B, was also unsuccessful on test because of low emission.

It is probable that the limit of our radical processing schedule has been reached. The last two tubes have been exhausted while bringing them to 750° C as rapidly as the automatic pressure control would allow. This control limits the system pressure to 3×10^{-4} mm Hg. Figure VIII-1 shows a composite temperature record for the MF-12B magnetron. Figure VIII-2 shows the pressure record for the period marked A as the tube comes up to cathode breakdown temperature. The pressure oscillates between 10^{-5} and 3×10^{-4} mm Hg. These oscillations are caused by the operation of the automatic control. They cease after breakdown is completed, and the temperature remains constant, while the pressure gradually decreases to an equilibrium value. Figure VIII-3 is the pressure record for period B in Fig. VIII-1, where breakdown is completed.

A post-mortem examination of the MF-9B magnetron showed the cathode coating to be puffy and nonadherent to the mesh. While this may have been due to the leak mentioned above, it is very likely that the bakeout was too rapid.

Magnetron MF-10B has been extensively tested in order to determine its power limitations. Unaccountably an efficiency of only 25 percent could be achieved, and the tube refused to operate at high values of magnetic field. A peak input power of 12 Mw was observed for 1-μsec pulses, but the output was only about 2.5 Mw peak and 500 watts average power. In view of the fact that the cathode was behaving well at this input level and that extensive cold tests had verified the adequacy of the output circuit, it is suspected that end-space resonances may be responsible for the power limitations.

A Rieke diagram, run at moderate power level, shows the pulling figure to be very low and the constant power contours to be badly distorted. Accordingly, a last effort is being made to modify the end-space geometry by a radical increase in the size of the cathode end shields. The final two tubes will be tested with this change.

Recent magnetron processing schedules have disclosed a structural weakness in the design of the anode end plate ring joint which tends to open up as the tubes cool down after high temperature bakeout. The design has now been changed, so that the steel end

plate ring is isolated from the copper anode by a copper sleeve capable of yielding and relieving thermal stress. The steel-to-copper joint is made with 1040° C gold solder; the copper-to-copper joint with BT solder.

The oxide cathode series of magnetrons has been extended to include two final tubes, MF-13B and MF-14B, both of which have gone through brazing assembly. Both of these tubes incorporate the new end plate ring design, and they will be assembled with oversize cathode end shields. The cathode coating for these tubes is being modified by the addition of carbonyl process nickel powder to the standard carbonate mixture in equal proportions.

A final report on the high-power magnetron project is in preparation.

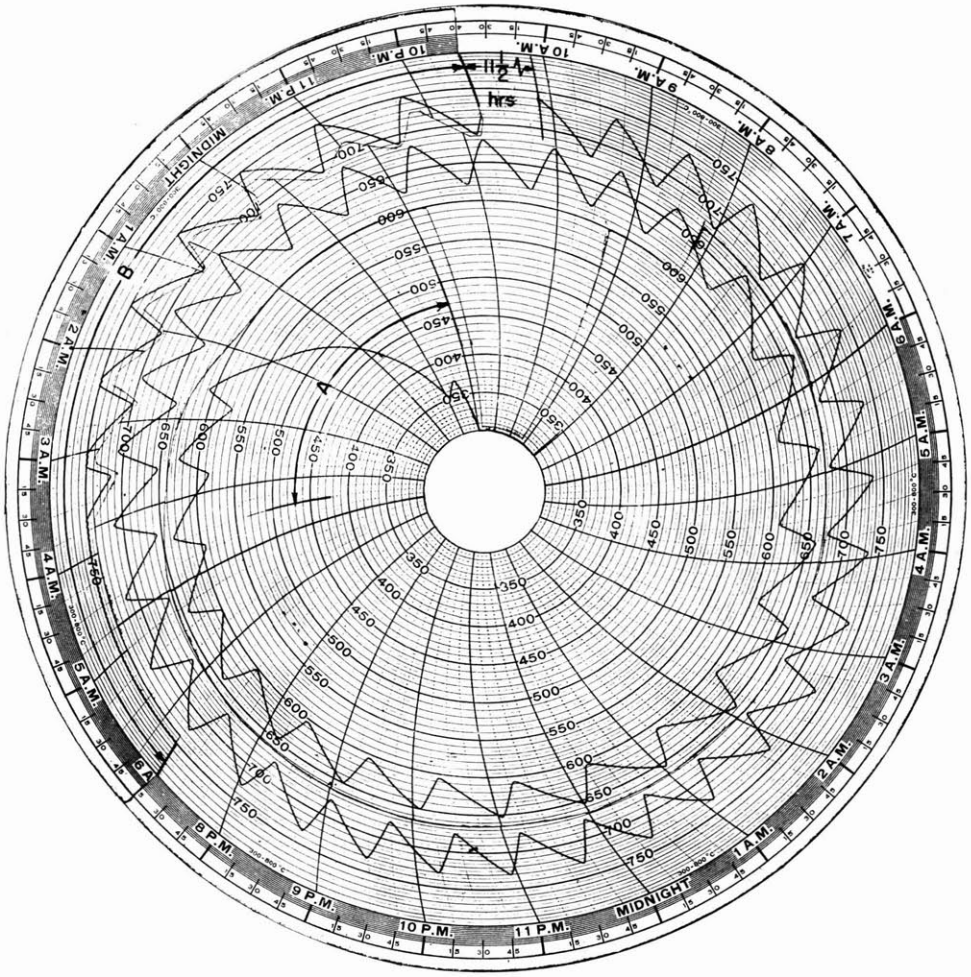

Fig. VIII-1
Temperature record of MF-12B processing schedule.

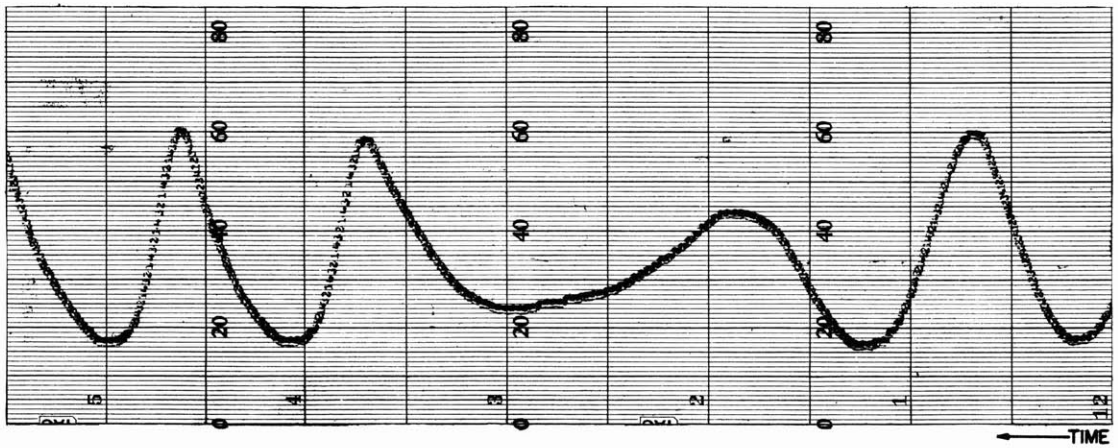

Fig. VIII-2

Magnetron MF-12B pressure record, period A.

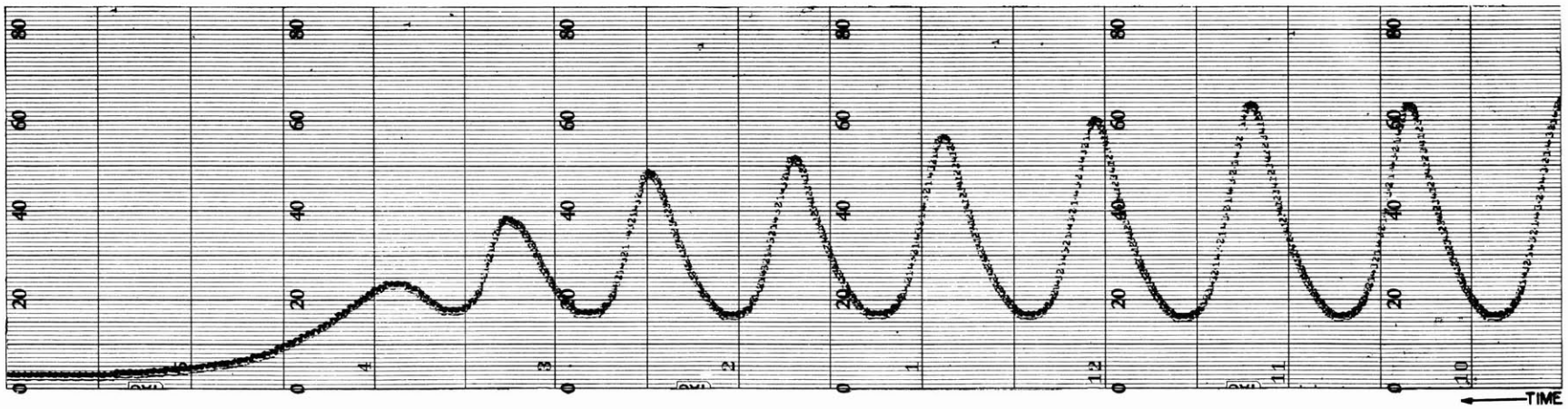

Fig. VIII-3

Magnetron MF-12B pressure record, period B: $20 = 10^{-5}$, $60 = 3 \times 10^{-4}$ mm Hg.

B. MICROWAVE TUBES

L. D. Smullin
Prof. L. J. Chu
A. D. Berk
A. W. Boekelheide
H. A. Haus
R. C. Knechtli
D. McKee
C. E. Muehe, Jr.
H. E. Rowe
C. R. Russell
L. Stark
A. Tonning

1. Noise and Space-Charge Waves

a. A multivelocity electron beam in a cylindrical drift tube

The behavior of an electron beam with velocity distribution and of finite transverse dimensions is found to be different in some respects from the behavior of a one-dimensional beam with the same velocity distribution.

The following assumptions have been made in the analysis:

1. An infinite magnetic field confines the motion of the electrons to the z-direction.
2. The velocity distribution f(v) is the same throughout the drift tube. There are no electrons traveling with a negative velocity.
3. The dc space charge is neutralized by ions.
4. The walls of the drift tube, which extends to $z = +\infty$, are perfect conductors.
5. Small-signal theory applies.
6. Short-range collisions are neglected.

The orientation of the coordinate system is shown in Fig. VIII-4. The field splits into TE and TM modes. The TM modes are linked to the electron current and are thus the only modes considered. All quantities are expanded in terms of the orthonormal set of functions $\phi_n(x, y)$ which satisfy the two-dimensional wave equation (1)

$$(\nabla_T^2 + k_n^2)\,\phi_n(x, y) = 0 \tag{1}$$

where ∇_T is the gradient in the transverse direction. The $\phi_n(x, y)$ are zero at the conducting boundary. The fields and the current have the following spacial dependence

$$\left.\begin{aligned} E_z(x, y, z) &= \sum_n E_{zn}(z)\phi_n(x, y) \\ \bar{E}_T(x, y, z) &= \sum_n E_{Tn}(z)\nabla_T\phi_n(x, y) \\ \bar{H}_T(x, y, z) &= \sum_n H_{Tn}(z)\left[\nabla_T\phi_n(x, y) \times \bar{1}_z\right] \\ J_z(x, y, z, v) &= \sum_n J_{zn}(z, v)\,\phi_n(x, y) \end{aligned}\right\} \tag{2}$$

where $\overline{E}_T$ and $\overline{H}_T$ are vectors in the transverse direction, and J_z is the current density per unit velocity of the incremental beam entering at z = 0 with a velocity in the range v, v + dv. A sinusoidal time dependence is assumed. The initial conditions are given at z = 0.

A Laplace transform is applied to the z dependence. The Laplace transform variable is p. Then, the determinantal equation for the nth mode, whose roots give the propagation constants, has the form

$$D_n(p) = 1 - \frac{k_n^2}{p^2 + \omega^2 \mu \epsilon} + \omega_p^2 \int \frac{f(v)dv}{(j\omega + vp)^2} = 0. \qquad (3)$$

The integral is extended over all velocity groups.

$$\omega_p^2 = \frac{e^2 n}{m \epsilon}$$

where n is the number of electrons per unit volume.

If the distribution function f(v) has only one maximum and is limited to a finite velocity range, a condition which will be presupposed from here on, the determinantal Eq. 3

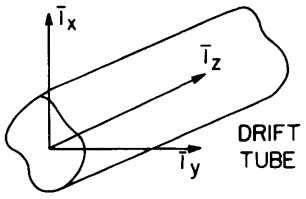

Fig. VIII-4
The coordinate system.

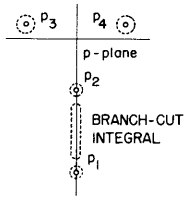

Fig. VIII-5
The roots in the p-plane.

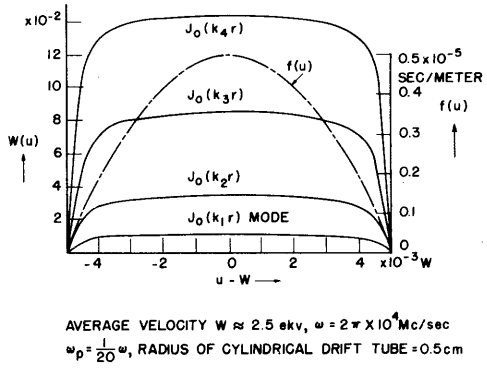

Fig. VIII-6
Plot of the weighting function.

has, in general, four roots. Two roots correspond to the cut-off modes of the guide; the other two roots are purely imaginary and correspond to the plasma waves of the single velocity beam. It can be shown that under the stated conditions there are no other roots to the determinantal Eq. 3. In the case of a one-dimensional beam, only two roots exist.

The function $D_n(p)$ has a discontinuity along the imaginary p axis for all values of $p = -j(\omega/v)$ for which $f(v) \neq 0$. Its value changes abruptly when passing from the positive-real half-plane of p to the negative-real half-plane. In addition to the residues at the roots of the determinantal equation, a branch-cut integral (2) appears in the complete solution for the current density per unit velocity. The residues and the path of integration along the imaginary p-axis are given in Fig. VIII-5. The increasing wave corresponds to a reflected wave and cannot be excited.

The current density per unit velocity has the form

$$J_{zn}(z, v) = \int J_{zn}(0, u)\, B_1(u, v)\, du\, e^{p_1 z} + \int J_{zn}(0, u)\, B_2(u, v)\, du\, e^{p_2 z}$$

$$+ \int J_{zn}(0, u)\, B_3(u, v)\, du\, e^{p_3 z} + \int J_{zn}(0, u)\, L(u, v, z)\, du \qquad (4)$$

where the last term is the contribution of the branch-cut integral. It can be shown that for large values of z, L(u, v, z) increases with the first power of z, if $v \neq u$, and with the second power of z, if $v \approx u$. This increase does not appear in the integral over all velocity groups, the total current density. The incremental currents $J_{zn}(z, v)dv$ in different velocity groups partly cancel, to give after integration of the last term in Eq. 4,

$$\lim_{z \to \infty} \iint J_{zn}(0, u)\, L(u, v, z)\, du dv = \int J_{zn}(0, u) \left[1 + \frac{k_n^2}{\left(\frac{\omega}{u}\right)^2 - \omega^2 \mu \epsilon} \right] \frac{e^{-j(\omega/u)z}}{D_{n+}\left(-j\frac{\omega}{u}\right)}\, du \qquad (5)$$

where $D_{n+}\left[-j(\omega/u)\right]$ is the value of the determinant $D_n(p)$ at

$$p = \lim_{\epsilon \to 0} \left(-j\frac{\omega}{u} + |\epsilon| \right).$$

It can be noted that the contribution of the branch-cut integral as given by Eq. 5 approaches zero for large z if $J_{zn}(0, u)$ is a continuous function of u. If noise is considered as an input, this is not the case and Eq. 5 will give a contribution to the mean-square fluctuations of the current. Further, it is found that the weighting function

$$w(u) = \left[1 + \frac{k_n^2}{\left(\frac{\omega}{u}\right)^2 - \omega^2 \mu \epsilon} \right] \frac{1}{D_{n+}\left(-j\frac{\omega}{u}\right)}$$

increases with increasing k_n. Figure VIII-6 illustrates the behavior of the weighting function for a special case. The importance of the branch-cut integral depends upon the amount of fringing of the electric field.

H. A. Haus

References

1. R. Q. Twiss: S.E.R.L. Tech. Jour. 1, 101, 1951
2. A. M. Clogston: Bell Telephone Laboratories, Memorandum MM-52-150-4, Feb. 1952

b. Calculation of noise in a finite diameter beam

Parzen (J. Appl. Phys. 23, 215, 1952) has presented an approximate method, utilizing the WKB method, for calculating the propagation of the lowest mode of a finite diameter electron beam in the gun region. This method is also applicable to the calculation of the higher beam modes. In this calculation it is assumed that the beam is in an infinite magnetic field which is always in the direction of electron motion, so that there is no sidewise motion of the electrons.

These methods are being applied to the problem of computing the noise standing wave in the drift space. A finite standing wave ratio is obtained, due to the excitation of the higher radially symmetric modes which have different wavelengths from the lowest mode. Calculations are being made for guns of constant perveance, but different angles of convergence and voltages, to determine how the absolute level and the standing wave ratio are affected by these factors.

H. E. Rowe

c. Experiments on noise in electron beams

Four electron guns have been operated in the demountable system described in previous Quarterly Progress Reports. The flow of positive ions to the inside wall of the tube has been measured by using a thin movable cylinder slightly smaller in diameter than the tube. In the magnetic field used, it was almost impossible for any electrons to reach this cylinder, so that the positive and negative ions could be collected and measured. From the measurements it was deduced that at the current, voltage, and pressure used (3 ma to 10 ma, 1000 volts to 1500 volts, and 0.3 to 1.0×10^{-6} mm Hg), the electron beam was fully neutralized except for a few centimeters near the anode, where the ions are pulled through the anode hole. Previously, the fact that there was full ion neutralization in the beam was deduced from measurement of the wavelength of the beam-diameter perturbations. This fact is now confirmed by the ion measurements.

The effect of a velocity-jump section on the noise current in the electron beam has

also been measured. The results are shown in Fig. VIII-7. The velocity of the electron beam was suddenly reduced, the beam was allowed to drift for a portion of a plasma wavelength, and then the velocity was suddenly increased to the original value. The positions and the magnitudes of the maxima and minima after the velocity-jump section were measured. The magnitudes are plotted in Fig. VIII-7 as a function of the position of the velocity-jump section. The theoretical curves were calculated by using a Smith chart and assuming that ac power is conserved in the beam.

It appears that the velocity-jump section acts like a section of transmission line of characteristic impedance Z_{02} inserted in a transmission line of impedance Z_{01}. The behavior of the minima differs considerably from the simple theory. It is not known why this is so, but higher beam modes may be the cause of the discrepancy.

The last experiment undertaken was measurement under the same conditions of noise current in an electron beam and noise figure of a helix as a function of distance along the beam. The results are shown in Fig. VIII-8.

D. A. Watkins (Technical Report No. 31, Electronic Research Laboratory, Stanford University, March 15, 1951) gives the following expression for the noise figure of a helix:

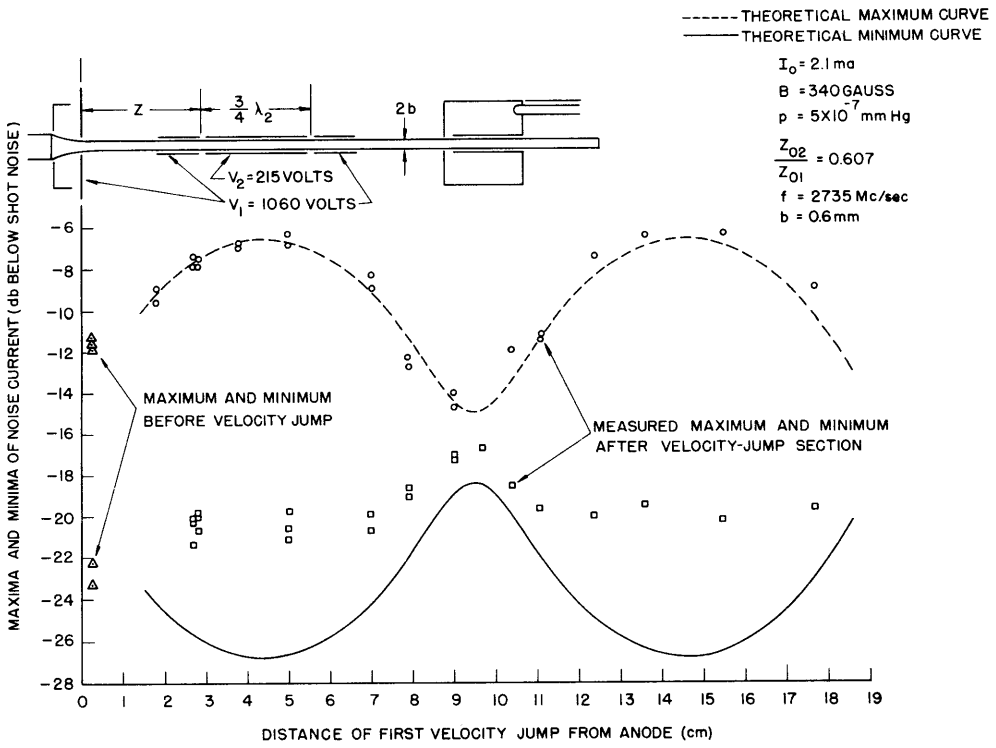

Fig. VIII-7

Noise current maxima and minima after a velocity-jump section.

$$F = 1 + \frac{I_o v_m^2}{2\eta C k T \Delta f} f(QC, d, \delta Z).$$

If the velocity modulation is replaced by the current modulation and an appropriate impedance factor, this expression becomes

$$F = 1 + \frac{4\eta e}{kT} \frac{V_o^2 \Gamma_m^2}{\lambda_q^2 f^2 C} f(QC, d, \delta Z)$$

where Γ_m^2 is the value of the maximum mean-square noise current below shot noise. All other quantities are those defined by Watkins.

The equations above apply to a beam with an infinite standing wave ratio of ac current and velocity. Let us assume a velocity modulation of the form

$$v = v_{max} \cos \beta Z \pm j v_{min} \sin \beta Z.$$

This corresponds to ac power propagation in the beam, as the expression for v may be

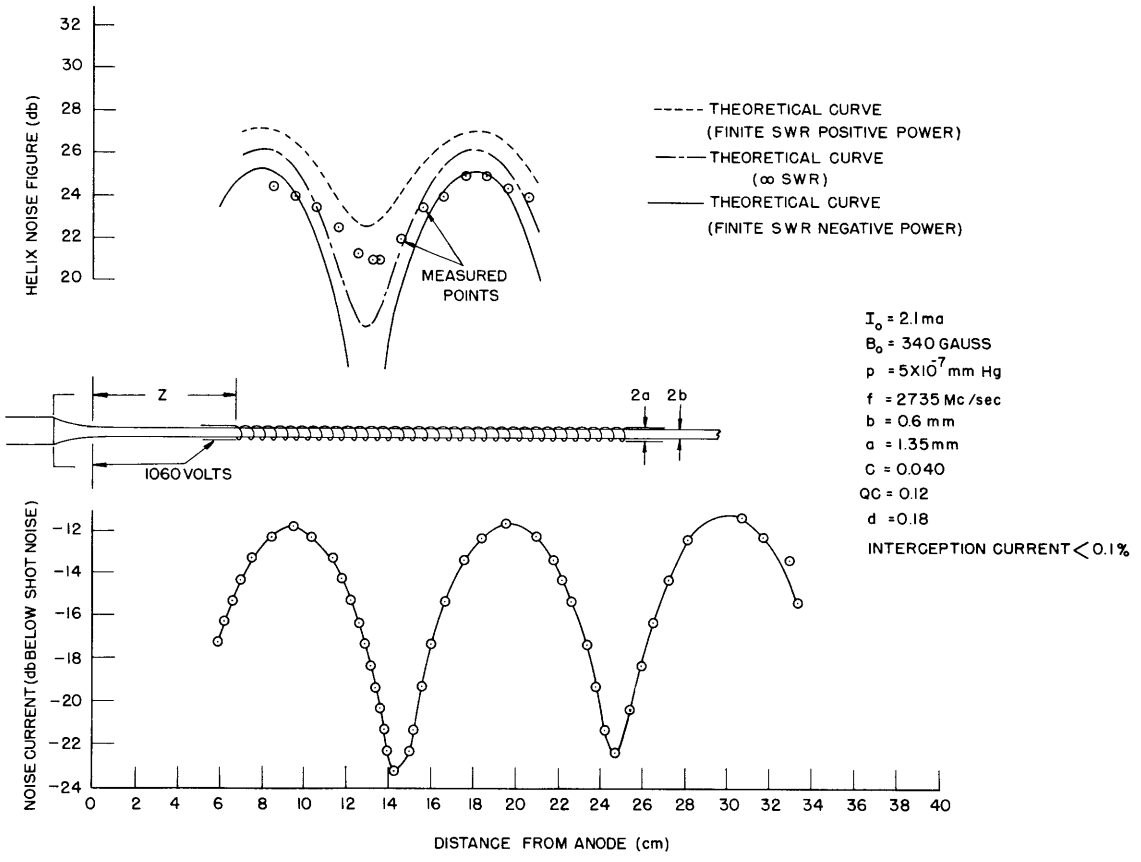

Fig. VIII-8

Noise current and noise figure vs distance from the anode.

written

$$2v = (v_{max} \pm v_{min})e^{j\beta Z} + (v_{max} \mp v_{min})e^{-j\beta Z}.$$

In transmission line theory, if the upper sign were used, power would be traveling to the left. In an electron beam this means that the faster wave is excited less strongly than the slower, or that positive ac power is flowing in the beam.

In this case the maximum and minimum values of the factor f(QC, d, δZ) in Watkins' expression for the noise figure become

$$f_{min} = \left[\sqrt{f'_{min}} \pm \rho\sqrt{f'_{max}}\right]^2$$

$$f_{max} = \left[\sqrt{f'_{max}} \pm \rho\sqrt{f'_{min}}\right]^2$$

where

f'_{min} = minimum value of f calculated on the basis of infinite SWR
f'_{max} = the maximum value of f calculated on the basis of infinite SWR

and

ρ = 1/VSWR of the velocity or current in the beam.

The positions of the minima remain unchanged.

The theoretical noise-figure curves of Fig. VIII-8 were computed by using the measured values of V_o, λ_q, f, Γ_m, ρ, and d, and the calculated values of C and Q. The value of C was checked by gain measurements at various currents in the helix. The gain always came out to within 2 db of the calculated value.

C. E. Muehe, Jr.

2. Traveling-Wave Amplifiers

a. Interleaved-fin slow-wave structure

The investigation of the interleaved-fin structure as a slow-wave circuit for traveling-wave amplifiers has been completed, and the results have been reported in a Master's Thesis, Dept. of Electrical Engineering, M.I.T. A forthcoming technical report will essentially reproduce the thesis material.

Two examples of calculated performance for this type of structure are given below. In both of these examples the wavelength λ_g of the synchronous space harmonic is large enough so that $L/\lambda_g < 0.5$. In this range the impedance of the chosen space harmonic will be large as compared with that of the remaining space harmonics.

At a center frequency of 3000 Mc/sec, the pertinent performance data for the two cases are as follows:

	Case I	Case II
Beam voltage	14.0 kv	50 kv
Beam current	0.5 amp	28 amp
Beam diameter	0.125 inch	0.300 inch
L/λ_g	0.331	0.173
Circuit impedance	268 ohms	600 ohms
Gain parameter, C	0.113	0.35
Frequency bandwidth for amplification at constant beam voltage	7.5 percent	12 percent

The structures for cases I and II are shown in Figs. VIII-9 and VIII-10, respectively. In each case the structure geometry has been adjusted to give a wave velocity corresponding to the voltage tabulated above; under operating conditions these voltages will have to be increased somewhat.

L. Stark

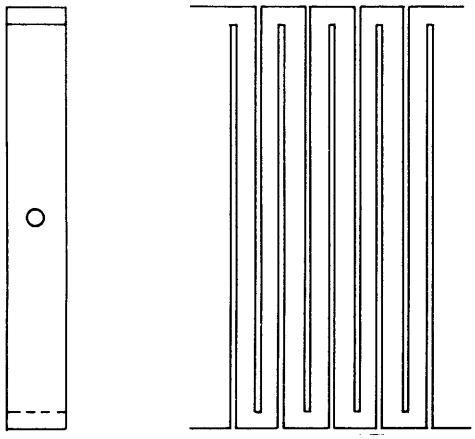

Fig. VIII-9
Structure for case I (actual size).

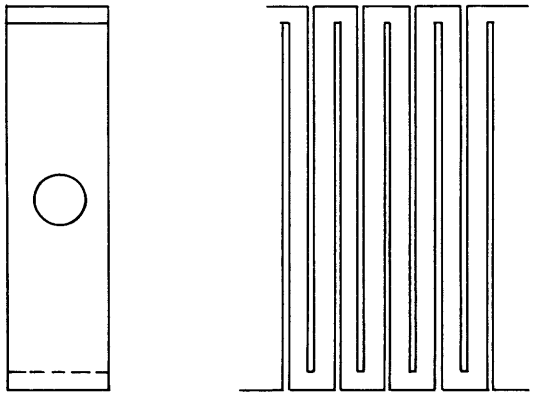

Fig. VIII-10
Structure for case II (actual size).

b. 10-cm pulsed traveling-wave amplifier

Before making a second high-power, pulsed, 10-cm tube, tests were carried out on the gun of tube No. 1 to obtain additional data. A new design of the gun structure was then attempted, using the electrolytic tank.

Gun tests. A photograph of the beam tester is given in Fig. VIII-11. A target of tungsten gauze was used, and the brass end plates were water-cooled.

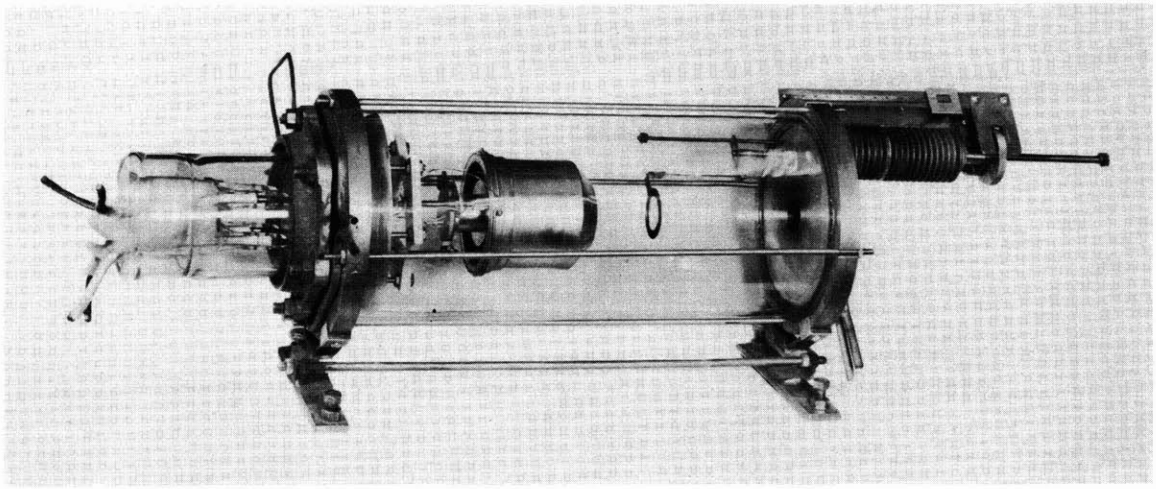

Fig. VIII-11
Beam tester.

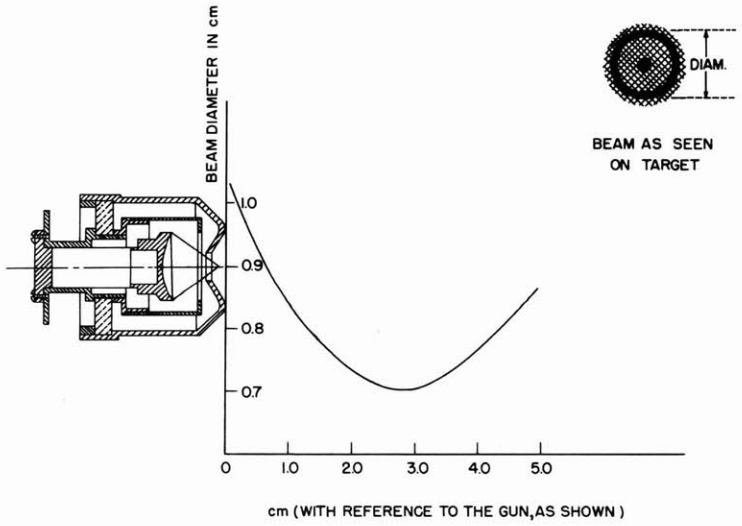

Fig. VIII-12
Beam-diameter-distance curve for gun from No. 1 tube.

For beam-diameter measurements, a pulse voltage of 14.7 kv was used. This gave a white-hot spot on the target, without damaging it, and also kept the X-ray radiation low. The beam-diameter-distance curve is shown in Fig. VIII-12. This curve differs considerably from the predicted values from the universal beam spread curve. This is thought to be due, primarily, to some fault in the original gun design, since we did not expect the coaxial type of beam actually obtained. At least qualitatively it can be said that the space-charge repulsion forces for the observed beam would be less than for a solid beam. In fact, the beam spread given is much slower than for a solid (uniform current density) beam.

Following this a check on the perveance was obtained, with the voltage run up to 15 kv. This gave a value of 2.52×10^{-6} amp/volts$^{3/2}$.

Tank experiments (Pierce gun). Two principal designs (Fig. VIII-13) were taken from the tank, using a scale multiplication factor of 5, a perveance of 2.49×10^{-6}, a gun half-angle $\theta = 37°$, and a ratio of (radius of cathode sphere)/(radius of anode sphere) = 2.28 (values equal to, or close to, those already adopted in the original design).

C. R. Russell

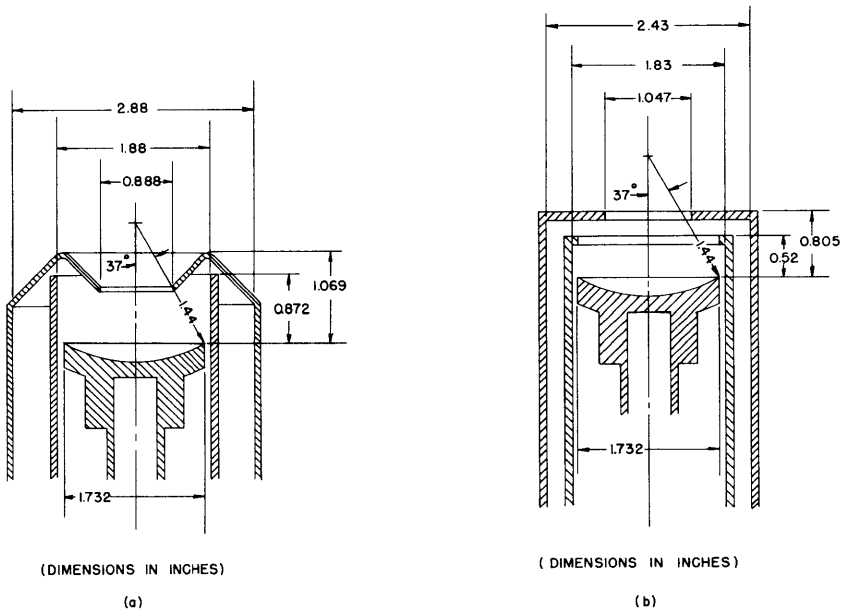

Fig. VIII-13
Electron gun designs taken from the tank.

c. Helix surrounded by a resistance sheath

Calculations have been made of wave propagation along a helix surrounded by a resistive sheath. Approximate formulas for attenuation and phase-constant have been derived. The results will be published in forthcoming Technical Report No. 232.

A. Tonning

3. 1-Mev Pulsed Electron Source

A solution has been obtained for Poisson's equation which is applicable to relativistic space charge limited electron flow between parallel-plane electrodes. With the substitution of the relativistic expression

$$v = c\left[1 - \frac{1}{\left(1 + \frac{eV}{m_o c^2}\right)^2}\right]^{1/2}$$

into the one-dimensional form of Poisson's equation

$$\nabla^2 V = \frac{d^2V}{dz^2} = -\frac{\rho}{\epsilon} = -\frac{J}{\epsilon v}$$

and after expansion into series form and integration, one obtains

$$z = \frac{1}{3}\left(\frac{2^5 e \epsilon^2 V^3}{J^2 m_o}\right)^{1/4}\left(1 - 0.107\phi V + 0.0426\phi^2 V^2 - 0.0234\phi^3 V^3 + 0.0150\phi^4 V^4 - \ldots.\right)$$

where V is the potential at a distance z from cathode, $\phi = e/(2m_o c^2)$, and all units are in the rationalized MKS system. The series is convergent for $\phi V < 1$, that is, for $V < 1.023 \times 10^6$ volts.

The first term of this series gives the usual nonrelativistic form of the Langmuir-Child equation. The correction of the subsequent terms amounts to approximately 8 percent at 1 Mv. However, an unreasonably large cathode-anode spacing is required to satisfy this expression with the desired characteristics.

The gun design used up to this point was also so large that the glass envelope and Kovar-glass seal were too big to fabricate with our available facilities. It was decided, therefore, to redesign the electron gun as a variation from the Pierce design. Pierce calculations were used to establish the electric field near the cathode and out to approximately one-tenth of the anode voltage. In this way, a smaller diameter cathode electrode and anode, as well as a shorter cathode-anode spacing, could be used. Since the field beyond the $1/10\ V_o$ point was unknown, it was obtained from an electrolytic plot of a half-section of the gun (ignoring space charge). The resultant beam shape could then be traced all the way to the anode.

With this technique it now appears feasible to make a gun of reasonable dimensions that will produce a diverging beam so that the current density at the metal-foil window will be reasonably low. This will eliminate the need for the magnetic focusing coil required in our original design.

A. W. Boekelheide

4. Injected Beam Magnetrons

In a technical report which is in preparation, it will be shown that magnetrons with an injected beam have some interesting properties that make them particularly suitable for operation at high frequencies (10^{10} cps or greater). We shall summarize here the major theoretical and experimental results developed in the technical report.

It is known that, for a given type of magnetron and a given operating point on the reduced performance chart, we have (see ref. 1, p. 435)

$$r_a \approx \lambda; \quad B \approx \frac{1}{\lambda}$$

where r_a is the anode radius, and B is the magnetic induction. Both of these requirements become impractical for decreasing λ. On the other hand, if we do not keep r_a/λ constant, we shall have to adjust V_a and I_a, the dc anode voltage and current, according to the following laws (see ref. 1, pp. 233, 416 and 455) in order to stay in a region of acceptable efficiency on the performance chart

$$V_a \approx \left(\frac{r_a}{\lambda}\right)^2; \quad I_a \approx \left(\frac{r_a}{\lambda}\right)^2 \cdot \left(\frac{h}{\lambda}\right)$$

where r_a is the anode radius of the magnetron, and h is the anode height (dimension parallel to the cathode). The total input power P (average power) has the following dependence on the ratios

$$P \approx \left(\frac{r_a}{\lambda}\right)^4 \cdot \left(\frac{h}{\lambda}\right).$$

This shows that with increasing frequency we tend, in conventional magnetrons, to work at increasingly high-power levels, and we are faced with either of two problems: (a) for high-power magnetrons, to find a way of handling higher powers and higher voltages in smaller structures; and (b) for low-power magnetrons, to find a structure which, unlike the conventional ones, can work with fair efficiency in the very low power region of its performance chart.

In the case of high-power magnetrons, the difficulties in a conventional structure will essentially be (a) avoiding flashing at the cathode and (b) dissipating higher thermal losses in smaller structures. (This includes the problem of dissipating the back-bombardment power which tends to overheat the cathode.)

Considering that flashing is due to both the back-bombardment and the higher electric field on the emitting surface, we may avoid both by moving the emitting surface out of the interaction space. This suggests using a structure with an injected beam, without electronic emission in the interaction space. This idea has been tried at relatively low frequencies by Helbig (3) and at microwave frequencies by A. M. Clogston at the Bell Telephone Laboratories.

Up to now, we have mainly concentrated our work on the problem of low-power c-w magnetrons with injected beams.

We can define an rf voltage V_1 proportional to the rf field and an rf current I_1 proportional to the electronic current (see ref. 2, p. 190) in the interaction space. In conventional structures the rf current I_1 has a large magnitude, practically independent of V_1 and of the load (see ref. 2, pp. 357-359). Therefore, we can represent the electron beam in an equivalent circuit by a constant current generator in parallel with a susceptance jB, where the latter accounts for the complex character of the electronic conductance. We then get the approximate equivalent circuit of Fig. VIII-14 with $|I_1|$ approximately constant. The generated rf power P_1 is given by

$$P_1 = |I_1| \cdot |V_1| \cos \phi$$

where ϕ is the phase angle between I_1 and V_1. Operation at low power with large $|I_1|$ requires either small $|V_1|$ or small cos ϕ. However, if we define $a = |V_1|/V_a$, where V_a = dc anode voltage, it can be shown that a lower limit is imposed on a by stability considerations. Moreover, a lower limit is imposed upon V_a, and it can be shown that for frequencies increasing over a certain limit (approximately 10^{10} cps) we cannot avoid increasing V_a. Hence, in the last analysis, we find that we are bound by a lower limit, too, for $|V_1| = aV_a$ in conventional magnetrons. (In magnetrons with injected beams, we can find structures in which more favorable stability conditions allow a lower a, that is, a lower $|V_1|$. This is one way in which injected beam magnetrons appear more suitable for low-power operation.) Therefore, in conventional magnetrons, low-power operation means operation at high current $|I_1|$, high voltage $|V_1|$, and small cos ϕ. This can be seen to result in high losses (inefficiency) and poor frequency stability (operation far away from the natural resonance of the cavity).

Further, in magnetrons with injected beam, it is possible (in contrast with the conventional structures) to control the electronic current density and, by this, to keep $|I_1|$ as small as we desire. Therefore, instead of operating inefficiently and with poor stability at high $|I_1|$ and low cos ϕ, we can operate at low current and large cos ϕ. This characteristic is the feature which makes injected-beam magnetrons suitable for low-power operation.

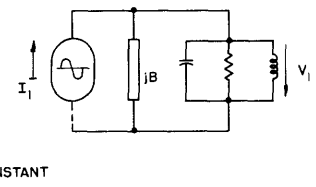

Fig. VIII-14
Magnetron equivalent circuit.

Practically, different structures with injected beam seem possible. Figures VIII-15 to VIII-17 show some of them. Structures of the type sketched in Fig. VIII-15 are expected to show poor control of the velocity of the electrons in the interaction space, because this velocity depends upon the dc electric field which, in turn, depends upon the space charge confined between cathode and reflector. And may be expected, by comparison

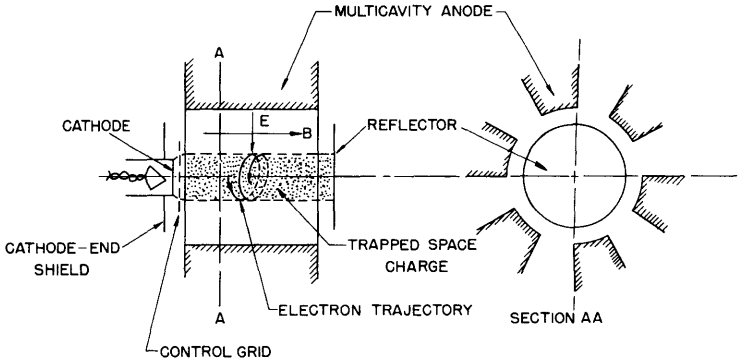

Fig. VIII-15

Injected-beam magnetron with no negative electrode (cathode) in the interaction space.

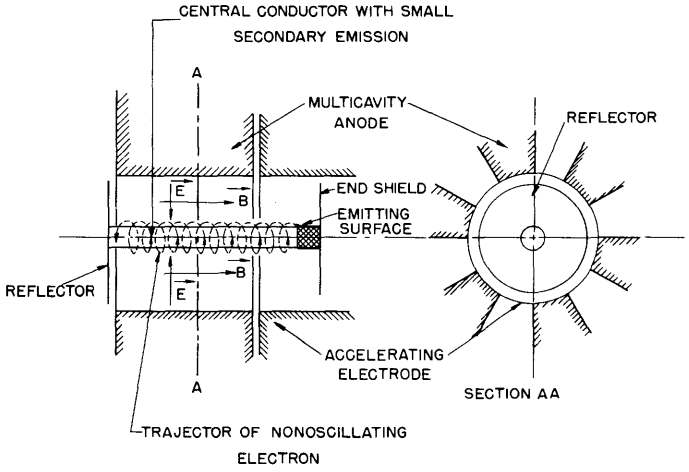

Fig. VIII-16

Injected-beam magnetron with cold cathode in interaction space.

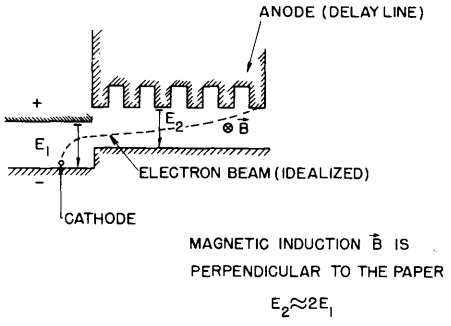

Fig. VIII-17

Linear injected-beam magnetron.

with the static (nonoscillating) behavior of the space charge of conventional magnetrons, that our space charge may be quite unstable. Since good control of the velocity of the electrons in the nonoscillating magnetron is an important element for stable operation of injected beam magnetrons (as will be shown in our technical report), we do not expect magnetrons like that shown in Fig. VIII-15 to yield particularly interesting results. (An analytical expression for the space charge in configurations of this type, even in the nonoscillating case, is not available.) In structures of the type illustrated in Figs. VIII-16 and VIII-17, we can keep the electronic current arbitrarily small, making the space charge in the interaction space of negligible importance for the dc electric field.* This shows interesting possibilities for controlling the electron stream in the interaction space by the dc electric field. Therefore, we expect these structures to lead to stable operation. Moreover, since leakage currents seem to depend, in general, upon the space charge, the fact that there is a smaller space charge in the interaction space will probably decrease the leakage current. This, in turn, will increase the efficiency of the structures of Figs. VIII-16 and VIII-17 at low-power operation.

Up to now, we have experimented on a magnetron of the type shown in Fig. VIII-15, made from a 725A-magnetron (X-band), from which the original cathode was removed and replaced by the cathode and reflector sketched in Fig. VIII-15. Although very weak oscillations were observed in pulsed operation, it was possible to prove that they were of the traveling-wave type. Further, very high leakage currents were observed; they were found (after destruction of the tube) to be due, essentially, to a mechanical distortion of the reflector. Moreover, considerable reflector current (even with the reflector 90 volts below the cathode) was observed in dc operation. This current probably is due to the electronic interaction resulting from noise amplification within the electron stream. A theory of this mechanism in the case of a linear structure similar to that shown in Fig. VIII-17 has been outlined by Buneman (4) and may apply, with some algebraic modifications, in the case of cylindrical structures. Unusually high emission ($1 A/cm^2$) was observed without notable shortening of the life of the cathode. This also could be explained by the same interaction, producing a back-bombardment on the cathode, even outside the interaction space and without oscillation of the desired frequency.

In order to minimize noise amplification we should, according to the theory of Buneman, decrease the space charge and control as closely as possible the velocity distribution within the electron stream, in order to approach a single velocity beam. (Indeed, the mentioned mechanism of amplification depends upon differences of velocities within dense electron beams.) Both of these aims can be approached by structures of the type shown in Fig. VIII-17. We hope in such structures to reduce the leakage

*Structures of the type shown in Fig. VIII-16 were first suggested by Clogston at Bell Telephone Laboratories.

currents to the anode and back toward the cathode or the reflector. This should also increase the efficiency at low power, as we have mentioned.

The tube mentioned above is now being reassembled with the reflector in the correct position. Further experiments will be made on structures of the type illustrated in Figs. VIII-16 and VIII-17.

R. Knechtli

References

1. G. B. Collins: Microwave Magnetrons, McGraw Hill, 1948
2. J. C. Slater: Microwave Electronics, Van Nostrand, 1950
3. A. Helbig: Hochfreq. u. Electroak. 50, 3, 1937
4. O. Buneman: Generation and Amplification of Waves in Dense Charged Beams under Crossed Fields, Nature, March 25, 1950, p. 474

5. The Use of Ferrites at Microwave Frequencies

The recent articles of Polder, Hogan, and Luhrs have pointed out that certain of the ferrites may have very important microwave applications. The use of the ferrites as gyrators promises to be their most important microwave application. Other possible applications are as magnetically controlled attenuators or switches.

It was decided to approach the use of ferrites by studying both their circuit applications and their fundamental properties. Part a below describes some experiments in building an X-band gyrator and a circulator. Part b outlines a theoretical study being undertaken to determine the properties of a ferrite sample from its effect on a resonant cavity.

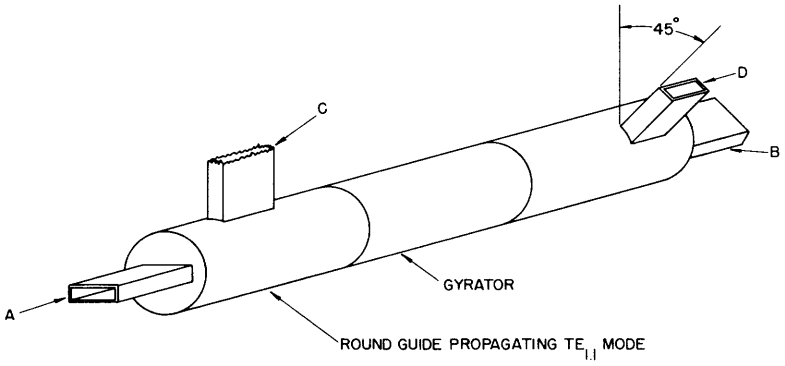

Fig. VIII-18

Microwave circulator using a ferrite gyrator to produce a 45° rotation of the plane of polarization on each transit.

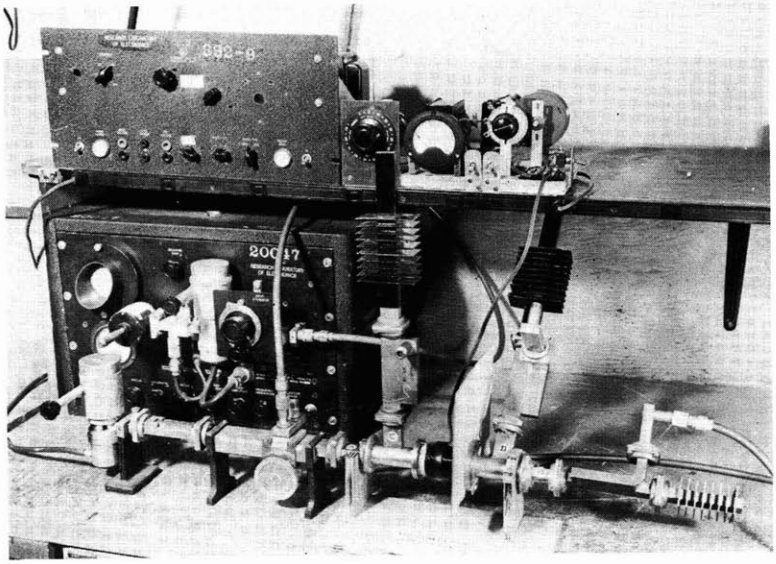

Fig. VIII-19
Microwave circulator.

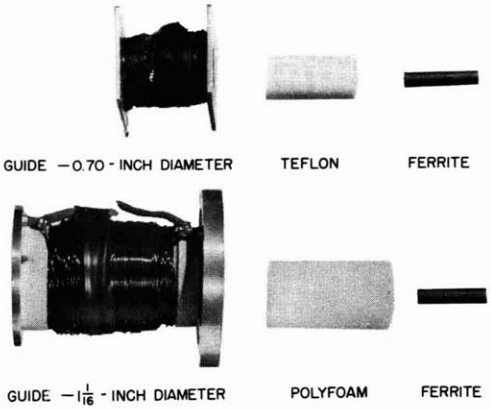

Fig. VIII-20
Microwave gyrators.

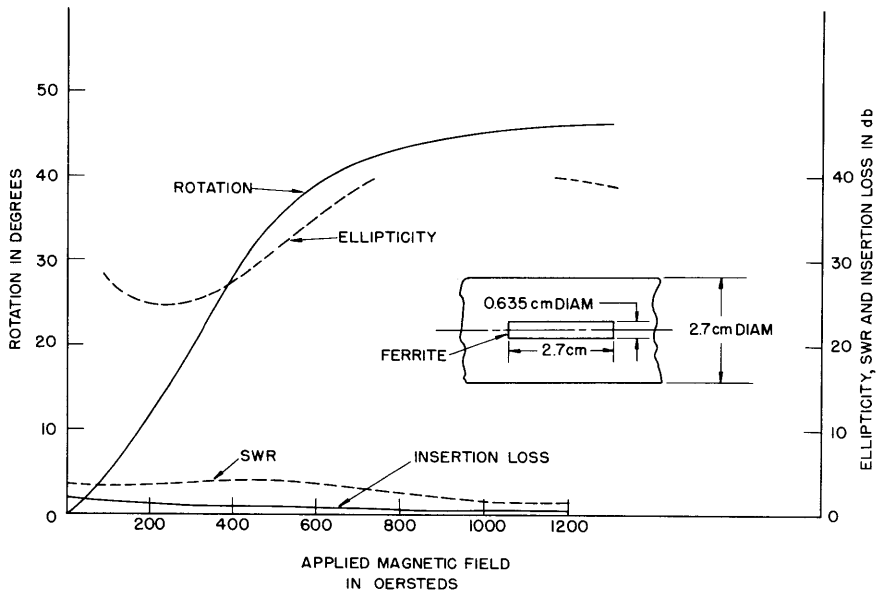

Fig. VIII-21

Properties of ferrite vs applied magnetic field.

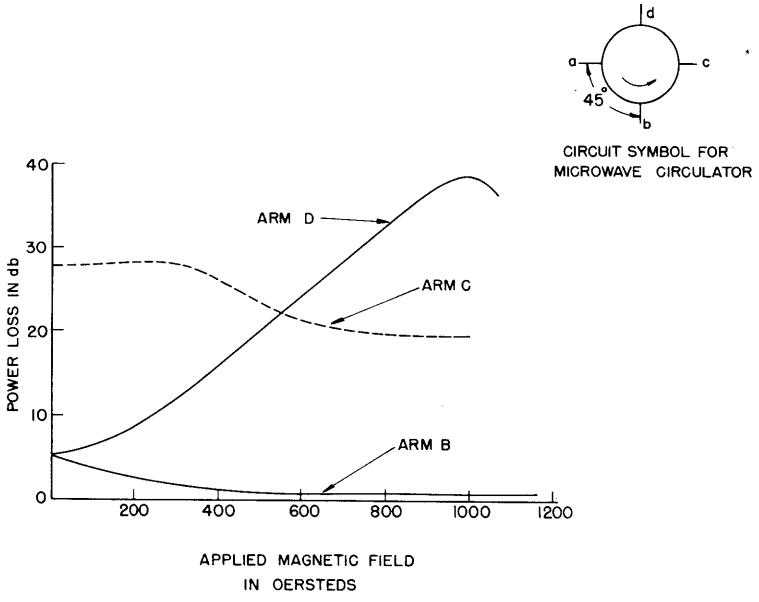

Fig. VIII-22

Output of circulator arms vs magnetic field; the frequency is 9240 Mc/sec.

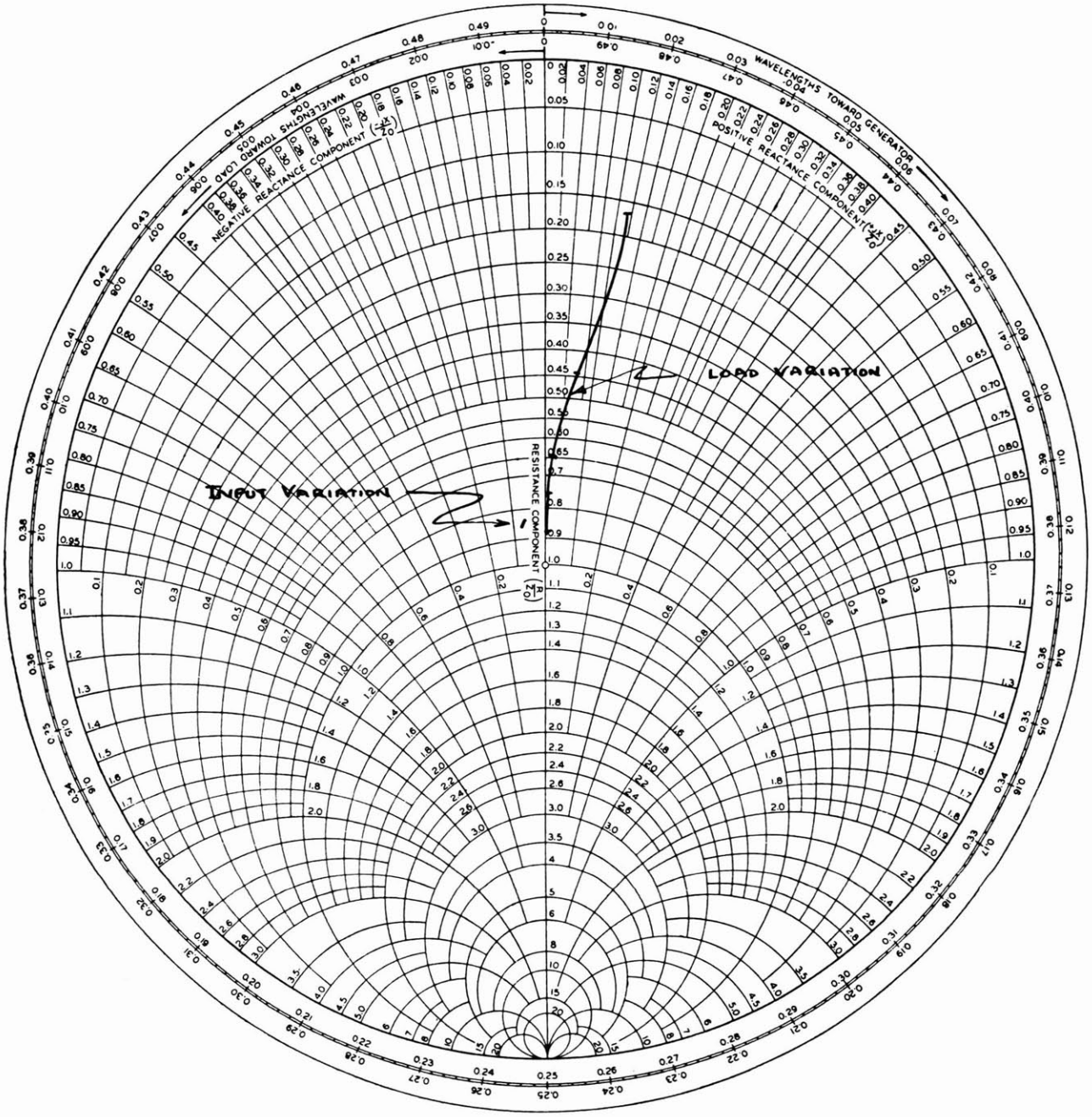

Fig. VIII-23
Circulator input impedance vs load impedance.

(VIII. TUBE RESEARCH AND DEVELOPMENT)

a. Development of an X-band circulator

(The following is a brief abstract of a Master's thesis for the Department of Electrical Engineering, M.I.T. carried out by D. A. McKee in this laboratory during the past quarter.) The problem was to design and build a 3-cm circulator using available ferrite rods. The ferrites used were obtained from the C. H. Luhrs Company, and were made by General Ceramics Company.

Figure VIII-18 is a diagram of a circulator. Arms A and C, and arms B and D, couple to mutually perpendicular TE_{11} modes in the round guide. B is rotated 45° from the plane of A. The gyrator is a round waveguide with a ferrite rod lying along the axis. An external solenoid produces an axial dc magnetic field through the ferrite. As shown by Polder this has the effect of rotating the plane of polarization of a plane wave incident on the ferrite. The size of the ferrite rod and the magnetic field strength are adjusted to cause a rotation of 45° on one passage through it. Thus, a signal injected at A will come out of B, a signal injected at B will come out of C, etc.

Figure VIII-19 is a photograph of an X-band circulator. Figure VIII-20 is a photograph of two gyrators. The upper unit is one made by C. H. Luhrs Company, the bottom unit was made in our laboratory and was used in most of our experiments. Figure VIII-21 shows the rotation of the plane of polarization, ellipticity, input standing wave ratio, and insertion loss vs applied dc magnetic field. These data were characteristic of the gyrator used in the circulator.

Figure VIII-22 shows the performance of the circulator as a function of dc magnetic field. The finite coupling between arms A and C is due to internal reflections in the circulator. Figure VIII-23 shows the variation of the impedance, measured in arm A, caused by a large variation of the impedance connected across arm B.

Only preliminary high-power tests were made; their results may be summarized as follows. The ferrite rod, as used in our experiments, was thermally insulated by the polyfoam or teflon support. A temperature rise of approximately 25° C per watt of average power absorbed was found to exist. Since the insertion loss was approximately 0.6 db, the temperature rise due to an average transmitter power of 50 watts would be 186°C, which is in excess of the curie point of most ferrites. Thus, the loss must be reduced in order to keep down heating of the ferrite, and ventilation or cooling must be improved.

L. D. Smullin

b. Impedance of a cavity containing a generalized medium

A method of calculating the impedance of a cavity given by J. C. Slater (1) is extended to the following problem involving overlapping modes.

Consider a cavity with two inputs, input 1 and input 2 for example, each in the form of a waveguide transmitting its own fundamental mode. Let input 1 be coupled to a

cavity mode α, and input 2 to another cavity mode β. Consider further that the α and β modes are coupled together, due to the presence of a generalized medium in the cavity, and that all other cavity modes have negligible amplitudes. (A generalized medium is one that can be described in terms of the complex tensor quantities ϵ, the permittivity (or an equivalent σ, the conductivity), and μ, the permeability; both of which may be inhomogeneous.) The following treatment will be restricted to a medium for which σ alone has generalized properties.

The electric field in the cavity is given, by hypothesis, by

$$\vec{E} = A_\alpha \vec{E}_\alpha + A_\beta \vec{E}_\beta \tag{1}$$

where $\vec{E}_\alpha$, $\vec{E}_\beta$ are the two dominant cavity modes and A_α, A_β are their respective amplitudes, satisfying

$$(k_\alpha^2 - k^2)A_\alpha = -j\omega\mu \left[\int_{\text{vol.}} \vec{E}_\alpha \cdot \overleftrightarrow{\sigma} \cdot \vec{E}\, dv - \int_{\text{surf.}} \vec{n} \times \vec{H} \cdot \vec{E}_\alpha\, ds \right] \tag{2}$$

$$(k_\beta^2 - k^2)A_\beta = -j\omega\mu \left[\int_{\text{vol.}} \vec{E}_\beta \cdot \overleftrightarrow{\sigma} \cdot \vec{E}\, dv - \int_{\text{surf.}} \vec{n} \times \vec{H} \cdot \vec{E}_\beta\, ds \right]. \tag{3}$$

In Eq. 2 ω is the angular frequency of excitation, ω_α the unperturbed resonant angular frequency of the α cavity mode, $k = \omega/c$, $k_\alpha = \omega_\alpha/c$, and c is the velocity of light. The various symbols in Eq. 3 have analogous meanings. The surface integrals in Eqs. 2 and 3 are taken over a cross section of the input waveguides. If this cross section is taken sufficiently far from the cavity, H in Eq. 2 will be given by

$$\vec{H}_1 = i_1 Z_{c1} \vec{H}_{t1} \tag{4}$$

and in Eq. 3 by

$$\vec{H}_2 = i_2 Z_{c2} \vec{H}_{t2}. \tag{5}$$

$\vec{H}_{t1}$ is the transverse magnetic mode in the waveguide of input 1, Z_{c1} is its characteristic impedance, and i_1 is a coefficient representing the intensity of the excitation. Similar meanings are attached to symbols in Eq. 5. Finally, the transverse component of $\vec{E}_\alpha$ evaluated at the cross section of input 1 is given by

$$\vec{E}_{t\alpha} = v_{\alpha 1} \vec{E}_{t1} \tag{6}$$

where $\vec{E}_{t1}$ is the fundamental transverse electric mode in the guide of input 1, and $v_{\alpha 1}$ is a measure of the coupling between this mode and the mode $\vec{E}_\alpha$ of the cavity. For input 2, one has, similarly,

$$\vec{E}_{t\beta} = v_{\beta 2} \vec{E}_{t2}. \tag{7}$$

By solving for A_α and A_β from Eqs. 2 and 3 and substituting in Eq. 1, one obtains the field $\vec{E}$ in the cavity. Evaluating this field, first at the cross section of input 1 and equating it to $V_1\vec{E}_{t1}$, and then at the cross section of input 2 and equating it to $V_2\vec{E}_{t2}$, one obtains two equations which read, in matrix form

$$\begin{bmatrix} V_1 \\ V_2 \end{bmatrix} = \begin{bmatrix} Z_{11} Z_{12} \\ Z_{21} Z_{22} \end{bmatrix} \begin{bmatrix} i_1 \\ i_2 \end{bmatrix}. \tag{8}$$

The V's and the i's play the role of voltages and currents as shown in reference 1. Thus, the cavity under consideration can be regarded as a two terminal-pair network with an impedance matrix whose elements are

$$Z_{11} = \frac{v_{\alpha 1}^2}{\Delta}\left[\frac{k_\beta^2 - k^2}{j\omega\mu} + I_{\beta\beta}\right] \qquad Z_{12} = \frac{-v_{\beta 2} v_{\alpha 1} I_{\beta\alpha}}{\Delta}$$

$$Z_{21} = \frac{-v_{\alpha 1} v_{\beta 2} I_{\alpha\beta}}{\Delta} \qquad Z_{22} = \frac{v_{\beta 2}^2}{\Delta}\left[\frac{k_\alpha^2 - k^2}{j\omega\mu} + I_{\alpha\alpha}\right]$$

where

$$\Delta = \left[\frac{k_\alpha^2 - k^2}{j\omega\mu} + I_{\alpha\alpha}\right]\left[\frac{k_\beta^2 - k^2}{j\omega\mu} + I_{\beta\beta}\right] - I_{\alpha\beta} I_{\beta\alpha}$$

and

$$I_{\alpha\alpha} = \int_{\text{vol.}} \vec{E}_\alpha \cdot \vec{\vec{\sigma}} \cdot \vec{E}_\alpha \, dv$$

$$I_{\alpha\beta} = \int_{\text{vol.}} \vec{E}_\alpha \cdot \vec{\vec{\sigma}} \cdot \vec{E}_\beta \, dv$$

with analogous expressions for $I_{\beta\beta}$ and $I_{\beta\alpha}$. Note that, in general,

$$Z_{12} \neq Z_{21}$$

since $I_{\alpha\beta}$ will usually be different from $I_{\beta\alpha}$. In the case of magneto-ionic media it can be shown that for a suitable geometry $I_{\alpha\beta} = -I_{\beta\alpha}$ and

$$Z_{12} = -Z_{21}$$

which is the basic property of a gyrator (2).

A passive impedance Z_2 connected at input 2 is transformed at input 1, thus

$$Z_{\text{input 1}} = Z_{11} - \frac{Z_{12}Z_{21}}{Z_{22} + Z_2} . \tag{9}$$

In the case of magneto-ionic media, Eq. 9 then becomes

$$Z_{\text{input 1}} = Z_{11} + \frac{Z_{12}^2}{Z_{22} + Z_2} .$$

As a final application, the input impedance of a cavity with one input can be found by noting that $v_{\beta 2}$ reduces to zero and that consequently Eq. 8 reduces to a single equation, relating the current and the voltage at the input. The expression for this input impedance proves to be equal to Z_{11}, as previously given.

Remarks: The effect of the wall losses can easily be included in a more refined treatment. The effect of the cavity modes other than $\vec{E}_\alpha$ and $\vec{E}_\beta$ may also be included by adding to the impedance, already derived, a small term independent of frequency. Finally, it is noted that a similar treatment with similar results may be given in the case of media with generalized μ and isotropic ϵ (ferrites) (3).

A. Berk with B. Lax (Project Lincoln)

References

1. J. C. Slater: Microwave Electronics, Van Nostrand, 1950, Ch. IV
2. D. Polder: Phil. Mag. 40, 99, 1949
3. C. L. Hogan: The Microwave Gyrator, Bell System Telephone J. Jan. 1952